

How Accurately Can We Detect the Splashback Radius of Dark Matter Halos and its Correlation With Accretion Rate?

Enia Xhakaj¹★, Benedikt Diemer², Alexie Leauthaud¹, Asher Wasserman¹,
Song Huang¹, Yifei Luo¹, Susmita Adhikari³, Sukhdeep Singh⁴

¹*Department of Astronomy and Astrophysics, University of California, Santa Cruz, 1156 High Street, Santa Cruz, CA 95064 USA*

²*NHFP Einstein Fellow, Department of Astronomy, University of Maryland, College Park, MD 20742, USA;*

³*Kavli Institute for Particle Astrophysics and Cosmology, Stanford University, 452 Lomita Mall Stanford, CA 94305, USA*

⁴*Berkeley Center for Cosmological Physics, University of California, Berkeley, Berkeley, CA, USA*

Accepted XXX. Received YYY; in original form ZZZ

ABSTRACT

The splashback radius (R_{sp}) of dark matter halos has recently been detected using weak gravitational lensing and cross-correlations with galaxies. However, different methods have been used to measure R_{sp} and to assess the significance of its detection. In this paper, we use simulations to study the precision and accuracy to which we can detect the splashback radius with 3D density, 3D subhalo, and weak lensing profiles. We study how well various methods and tracers recover R_{sp} by comparing it with the value measured directly from particle dynamics. We show that estimates of R_{sp} from density and subhalo profiles correspond to different percentiles of the underlying R_{sp} distribution of particle orbits. At low accretion rates, a second caustic appears and can bias results. Finally, we show that upcoming lensing surveys may be able to constrain the splashback-accretion rate relation directly.

Key words: cosmology: theory – dark matter– methods: numerical

1 INTRODUCTION

In the standard Λ CDM universe, dark matter halos form hierarchically due to the collapse of dark matter overdensities. This process can be described by the self-similar spherical collapse model, in which overdensities are considered to be composed of infinitesimally thin mass shells. These shells expand due to the Hubble flow, decelerate, start collapsing gravitationally and eventually virialize (Fillmore & Goldreich 1984; Bertschinger 1985). The boundary between the virialized and infalling shells is known as the splashback radius. It is defined as the radius where dark matter particles reach the apocenter of their first orbit as they accrete onto dark matter halos (Diemer & Kravtsov 2014; Adhikari et al. 2014; Shi 2016). The splashback radius is associated with a sharp drop in the halo density profile that is created as particles pile up near the apocenters of their orbits. It has been argued that the splashback radius provides a physically motivated boundary to halos (Diemer & Kravtsov 2014; Adhikari et al. 2014; More et al. 2015).

Recent work has shown that a physically motivated

boundary is important for understanding the properties of both galaxies and halos. For example, Baxter et al. (2017) showed that the fraction of red galaxies in **redMaPPer** clusters (Rykoff et al. 2014) displays an abrupt decrease around the location of the splashback radius. It has also been shown that assembly bias is heavily dependent on halo mass definitions (More et al. 2016; Villarreal et al. 2017; Chue et al. 2018; Mansfield & Kravtsov 2019). Current halo finders use definitions of halo mass and halo radius based on somewhat arbitrary choices for the overdensity, Δ . As such, these standard halo mass definitions do not necessarily correspond to the virialized mass of the halo. More physically motivated definitions, such as the splashback radius, can conceal discrepancies in the assembly bias measurements (Chue et al. 2018). It has also been suggested that the splashback radius can be used to measure dynamical friction (Adhikari et al. 2016) and to constrain alternative theories of gravity and self-interacting dark matter (Adhikari et al. 2018; Banerjee et al. 2019).

★ E-mail: exhakaj@ucsc.edu

Recent theoretical interest in the splashback radius naturally raises the question of how well it can be measured in data. Based on the spherical collapse model, it has been suggested that the splashback radius can be approximated by the minimum in the slope of the density profile of dark matter halos (Adhikari et al. 2014; More et al. 2015). However, it is a common misunderstanding that the splashback radius is simply the ‘dip’ at the transition between the one and two-halo regime. Unlike the spherical collapse model, halos and their splashback boundaries are not spherical due to the scatter in particle apocenters (Adhikari et al. 2014; Mansfield et al. 2017). Furthermore, the energy and momentum of particles at infall can affect their splashback radius. As such, the steepest slope of the density profile is not necessarily the true splashback radius (Diemer 2017). Finally, systematics in optical observations of clusters can bias the location of the steepest slope (Busch & White 2017). However, being the closest observable, the location of the steepest slope has commonly been used as a definition of the splashback radius, especially in observations.

Previous studies have measured the splashback feature in stacked galaxy surface density profiles around massive galaxy clusters (More et al. 2016; Umetsu & Diemer 2017; Baxter et al. 2017; Chang et al. 2018; Shin et al. 2019; Contigiani et al. 2019; Zürcher & More 2019) and in weak lensing measurements (Chang et al. 2018). The detection of the splashback radius is achieved by comparing two model fits: a model with the splashback feature as introduced in Diemer & Kravtsov (2014) (the DK14 model) and a different ‘null’ model without a splashback feature.

DK14 uses the Einasto profile to describe the collapsed material (one-halo term) and a power-law profile for the infalling material (two-halo term) (Gunn & Gott 1972). More importantly, the model includes a truncation of the Einasto profile at r_t , which introduces a minimum in the slope of the density profile corresponding to the splashback feature.

The issue with the second ‘null’ model, is that there is no physical basis for a splashback-free halo in a Λ CDM universe. The splashback feature is a natural consequence of the hierarchical formation of dark matter halos (Fillmore & Goldreich 1984; Bertschinger 1985) so all dark matter halos should have a splashback radius. Hence, unless one is assuming a non- Λ CDM universe, there is no natural ‘null’ model with which to compare. *Instead of framing the detection issue as a model selection problem, we should be asking how precisely and accurately we can measure the splashback radius.*

In the following paragraphs we describe the methods used by More et al. (2016), Baxter et al. (2017) and Chang et al. (2018) to claim detection:

(i) More et al. (2016) were the first to claim a detection of the splashback feature in real data. They used the Sloan Digital Sky Survey (SDSS) DR8 data to measure surface density profiles around galaxy clusters using the **redMaPPer** cluster catalog. More et al. (2016) followed a model selection approach to determine the detection of the splashback feature. They defined an alternative DK14 model composed of a pure Einasto profile (setting $f_{\text{trans}} = 1$) and a power-law term to describe the density profile without a splashback feature. When compared to the splashback-free model, the original DK14 provided a better fit to the data. This sug-

gested that the data disfavored the splashback-free model, thus proving the detection of the splashback radius. More et al. (2016) defined the splashback radius as the steepest slope of their best fit DK14 profile.

(ii) Baxter et al. (2017) divided the collapsed and infalling regions of the density profile and studying only the collapsed part for the detection of the splashback radius. They chose the 1-halo term of the Navarro, Frenk, and White (NFW) profile (Navarro et al. 1996) to be the null splashback-free model. They used a Bayesian approach to fit DK14, including miscentering on the same dataset as More et al. (2016). They computed the location and steepness of the steepest slope by rebuilding the density profile and its log slope from the posteriors of their free parameters. Finally, they compared the slope of the DK14 fit collapsed region to that of the NFW fit. Because the collapsed region of DK14 was steeper than that of the NFW fit, they claimed a successful detection of the splashback radius.

(iii) Chang et al. (2018) detected the splashback feature around **redMaPPer** clusters with the first year of DES data using both surface density of galaxies and weak lensing profiles. Following the same approach as Baxter et al. (2017), Chang et al. (2018) demonstrated that the location and steepness of the collapsed term for the weak lensing profiles agreed with those measured from the stacked density profiles.

The goal of this paper is to study the accuracy and precision to which we can measure the splashback radius. First, we study how accurately we can measure the splashback radius from 3D density and subhalo profiles. We use results from **SPARTA** (Subhalo and Particle Trajectory Analysis), an algorithm that tracks particle trajectories to measure the splashback radius (Diemer 2017; Diemer et al. 2017). We compare the splashback radius measured with **SPARTA** with the location of the steepest slope of the density and subhalo profiles for a given halo sample. We consider scenarios in which halos are selected not only by mass but also by secondary halo properties such as halo mass accretion rate. This choice was motivated by previous work showing that the splashback radius is most strongly correlated with accretion rate (Diemer & Kravtsov 2014; Adhikari et al. 2014; More et al. 2015).

Second, we study how precisely we can measure the splashback radius from weak lensing data. Weak lensing is a direct probe of the mass profile of dark matter halos, and, thus, ideal for the detection of the splashback radius. We discuss how well we can constrain the correlation of the splashback radius with accretion rate at fixed halo mass for current surveys such as the Hyper Suprime Cam survey (HSC, Aihara et al. 2018), and future surveys like the Large Synoptic Survey Telescope (LSST, Ivezić et al. 2008), Euclid (Laureijs et al. 2011) and the Wide Field Infrared Survey Telescope (WFIRST, Spergel et al. 2013). Here, we only consider dark matter simulations without gas. We are also only studying the ideal case in which clusters have been correctly identified, without the impact of errors due to cluster finders or miscentering.

This paper is structured as follows. In Section 2, we introduce our halo and subhalo sample along with different definitions of the splashback radius. In this section, we also introduce the methods we use to compute and fit density,

subhalo, and weak lensing profiles. We present and discuss our results in Sections 3 and 4. Finally, we summarize our work in Section 5.

We adopt the cosmology of the MultiDark Planck 2 (MDPL2) simulation (Prada et al. 2012), namely, a flat, Λ CDM cosmology with $\Omega_M = 0.307$, $\Omega_b = 0.0482$, $\sigma_8 = 0.829$, $h = 0.678$, $n_s = 0.9611$, corresponding to the best-fit Planck cosmology (Planck Collaboration et al. 2014).

2 METHODS

2.1 Halo and Subhalo Selections

We aim to study cluster-sized halos similar to the sample used by Chang et al. (2018). We base our analysis on the publicly available MultiDark Planck 2 (MDPL2) simulation (Prada et al. 2012). We select halos from the ROCKSTAR halo catalog (Behroozi et al. 2013a,b) at $z = 0.36$. We pick host halos within a narrow mass range of $M_{200m} = 10^{13.8} M_\odot/h$ to $M_{200m} = 10^{14.1} M_\odot/h$. Both the mass range and the redshift correspond to the best fit halo mass of redMaPPer clusters with richness $20 < \lambda < 100$ and a redshift range of $[0.2, 0.55]$ in Chang et al. (2018).

Given that the location of the splashback radius is correlated with halo accretion rate (Diemer & Kravtsov 2014; Adhikari et al. 2014; More et al. 2015), we bin our halo sample by accretion rate. SPARTA and ROCKSTAR use different definitions for accretion rate over 1 dynamical time (Γ_{dyn}). Instead of using the definitions in the ROCKSTAR catalogs, we recompute Γ_{dyn} from the ROCKSTAR merger trees as in Diemer (2017):

$$\Gamma_{\text{dyn}} = \frac{\Delta \log M_{200b}}{\Delta \log a}, \quad (1)$$

where M_{200b} is the halo mass defined relative to an overdensity of $200\bar{\rho}$ where $\bar{\rho}$ is the mean matter density. Details about this process can be found in Xhakaj et al. (2019). SPARTA and ROCKSTAR employ different definitions for halo mass. Diemer (2017) measures M_{200m} using both bound and unbound particles while ROCKSTAR's default setting measures M_{200m} using only bound particles (see Xhakaj et al. 2019 for more information). Here we use the ROCKSTAR M_{200m} definition.

We neglect a subset (2%) of our halo sample that has negative mass accretion rates. These could be mergers or fly-bys. After selecting host halos with $10^{13.8} < M_{200m} < 10^{14.1} M_\odot/h$ and removing halos with negative accretion rates, our final sample consists of roughly 25000 halos.

We divide this catalog by mass accretion rate such that each bin contains an equal number of about 5000 halos. Each sub-sample has a similar mass distribution (Figure 1). Our accretion rate bins are $[0, 1.1, 1.8, 2.5, 3.4, 13.1]$.

We also study the 3D profiles of subhalos around our $M_{200m} = 10^{14} M_\odot/h$ halo sample (see Section 3.2). We consider subhalos that will host galaxies from the upcoming DESI (Dark Energy Spectroscopic Instrument) experiment (DESI Collaboration et al. 2016). The DESI Bright Galaxy Sample (BGS) is a flux-limited sample selected with an r-band magnitude threshold of 19.5 (Omar Ruiz Macias et al. *in prep*). We select subhalos within the mass bin $10^{12} < M_{\text{peak}} < 10^{12.06} M_\odot/h$. The number density of this sample is $\bar{n} = 10^{-3} \text{Mpc}/h$ at a redshift of 0.36, which matches

the expected number density of BGS. We also want the subhalo sample to reflect the Y1 area that will be covered by DESI. For this purpose, when studying subhalo profiles, we limit the volume used to extract profiles to the expected DESI Y1 area (comoving volume of $0.6 (\text{Gpc}/h)^3$).

2.2 Splashback Radius Modeling and Definitions

We now introduce various definitions of the splashback radius that have been used in previous work. We also discuss how previous work has modeled and measured the splashback radius. In this paper, the splashback radius is denoted as R_{sp} .

2.2.1 Splashback Radius from Particle Dynamics

SPARTA measures particles' apocentric radii by tracing their trajectories and thus provides a direct measurement of the splashback radius (hereafter R_{SPARTA}) (Diemer 2017; Diemer et al. 2017). SPARTA has not been run on MDPL2. To obtain SPARTA based determinations of the splashback radius, we match our MDPL2 halo sample with that of the L500-Planck simulation at the same redshift ($z = 0.36$). L500-Planck is a 500 Mpc box simulation with a Planck-like cosmology, on which SPARTA has already been run (Diemer & Kravtsov 2015; Diemer 2017). To obtain the distributions of R_{sp} for our sample, we make the same M_{200m} and Γ_{dyn} cuts in L500-Planck as for our MDPL2 sample at $z = 0.36$. Particles infalling onto halos have a range of apocentric radii. In order to have a more compact definition of R_{sp} , SPARTA catalogs provide the 50th, 63rd, 75th and 87th percentiles of the splashback radius measurements from individual particles. Hereafter we abbreviate SPARTA's n^{th} percentile measurement of the splashback radius as R_{SPARTA}^n .

This matching procedure is valid because (1) we have verified that Γ_{dyn} is identical (Xhakaj et al. 2019), and (2) we are interested in the statistics of R_{sp} in binned halo samples rather than R_{sp} of individual halos. The difference in resolutions between L500-Planck and MDPL2 will not affect our results, given that we are studying cluster outskirts, which are not affected by numerical artifacts.

2.2.2 Splashback Radius from Density Profiles

Another definition of the splashback radius is the location of the steepest slope of the density profile. This minimum in the slope roughly marks the separation of the collapsed and infalling regions of the halo.

We compute the logarithmic slopes of the profiles, both parametrically and non-parametrically, through the DK14 model and the Savitzky-Golay (SG) method (Savitzky & Golay 1964). The SG filter fits the profiles using a 4th order polynomial in radial bins (Diemer & Kravtsov 2014; More et al. 2015). The DK14 model describes the profile as comprised of 2 parts: a truncated Einasto profile, describing the collapsed region, and a power-law term, describing the in-

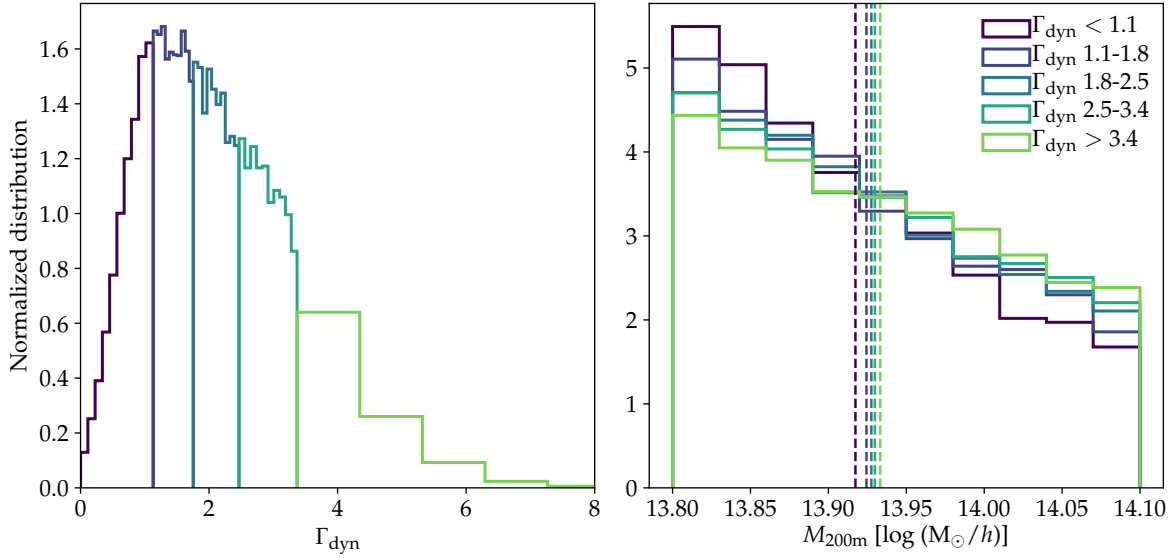


Figure 1. Left: Halo mass accretion rates of our five halo samples. Right: halo mass distributions of the same samples. Our five samples differ in their mean accretion rates but have similar mean halo masses (dashed vertical lines). Each bin has an equal number of halos and a similar mass distribution.

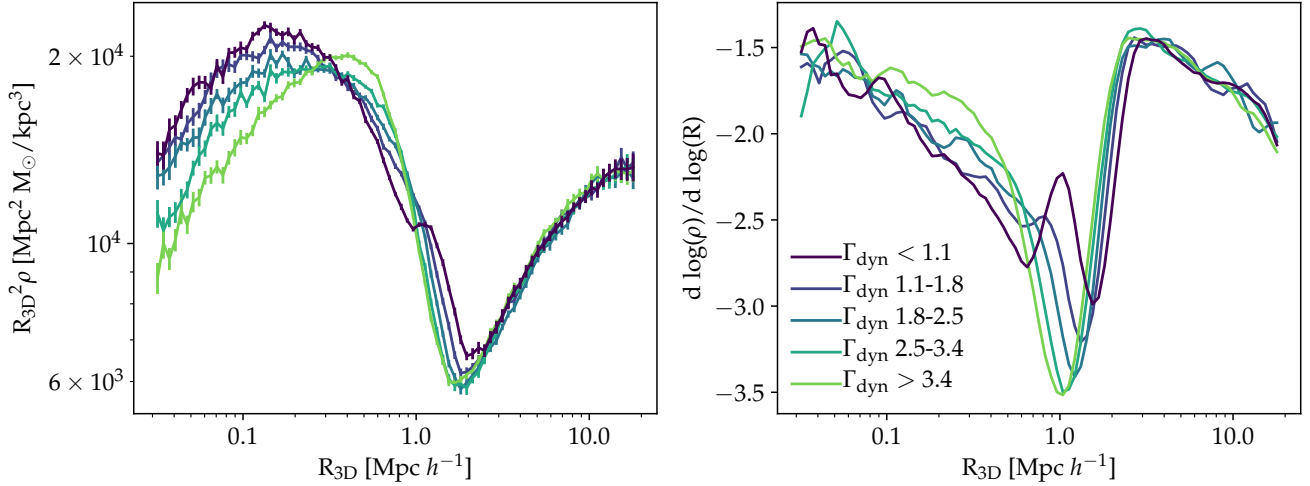


Figure 2. Left: 3D density profiles of our five samples with jackknife error bars (representing sample variance in the simulation). Each bin in accretion rate contains an equal number of halos. Right: corresponding logarithmic slopes of the profiles as computed using the Savtzyk-Golay filter. The minimum in the log slope varies with Γ_{dyn} . For low accretion rate halos, the appearance of a second caustic is apparent (blue and purple lines).

falling region of the halo:

$$\begin{aligned}
 \rho(r) &= \rho_{\text{infall}}(r) + \rho_{\text{coll}}(r) \\
 \rho_{\text{coll}}(r) &= \rho_{\text{Ein}}(r) f_{\text{trans}}(r) \\
 \rho_{\text{Ein}}(r) &= \rho_s \exp\left(-\frac{2}{\alpha} \left[\left(\frac{r}{r_s}\right)^\alpha - 1\right]\right) \\
 f_{\text{trans}}(r) &= \left[1 + \left(\frac{r}{r_t}\right)^\beta\right]^{-\gamma/\beta} \\
 \rho_{\text{infall}}(r) &= \rho_0 \left(\frac{r}{r_0}\right)^{-s_e}.
 \end{aligned} \tag{2}$$

The truncation of the Einasto profile, implemented through

$f_{\text{trans}}(r)$, introduces a minimum in the slope of the density profile, which accounts for the steepening at R_{sp} . The model has 8 free parameters: ρ_s , the central scale density, r_s , the scale radius, α , the steepening of the inner slope of the Einasto profile, r_t , the truncation radius, β , the sharpness of the steepening, and γ , the asymptotic negative slope of the steepening term. The location of the steepest slope measured with the SG filter and the DK14 model are hereafter abbreviated as R_{SG} and R_{DK14} .

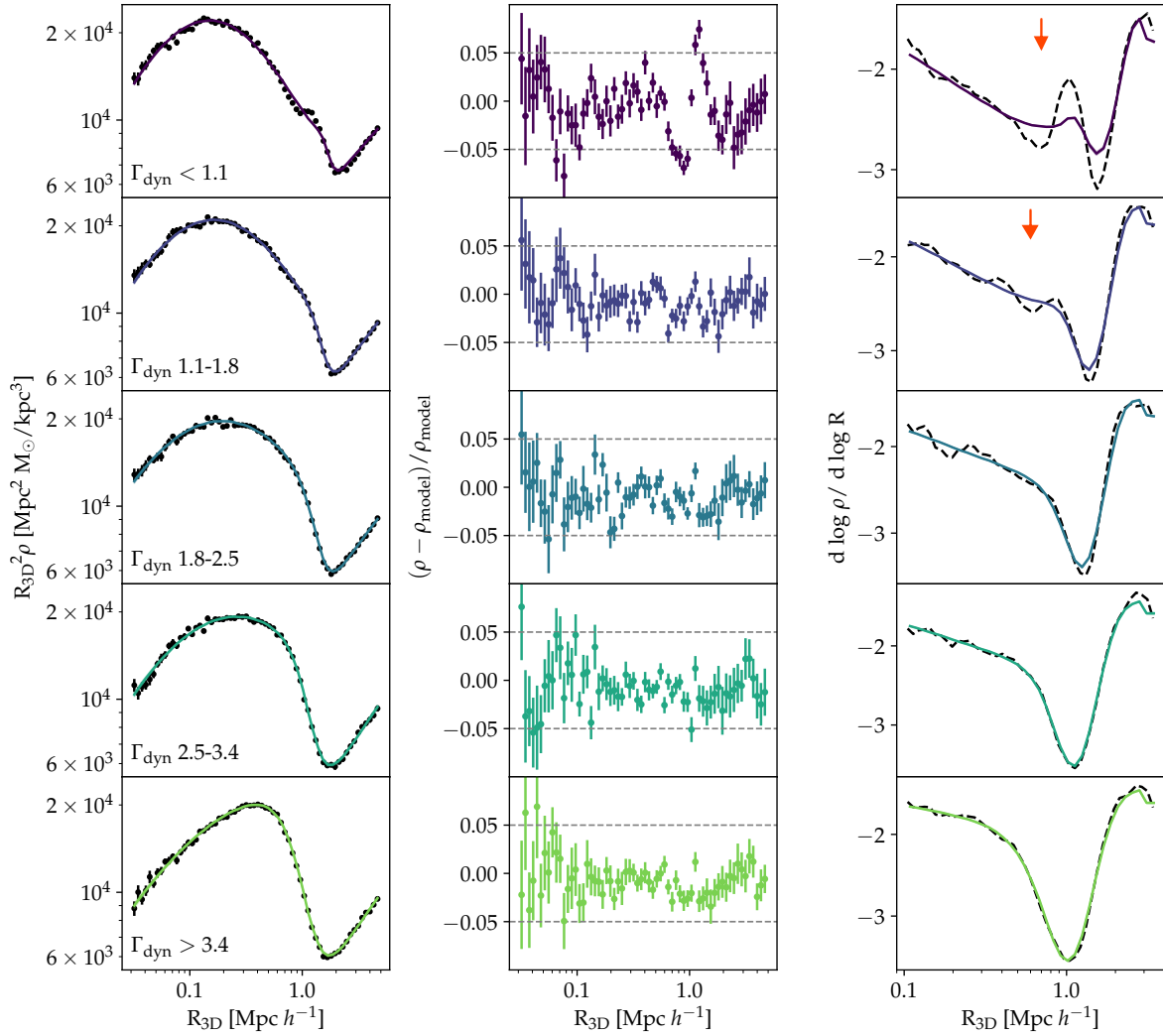


Figure 3. Left: best-fit DK14 models (colored lines) for ρ^{3D} measured in MDPL2 (black dots) in bins of accretion rate. Mass accretion rate increases from top to bottom while the mass of the halo sample is constant throughout all bins ($M_{200m} = 10^{14} M_{\odot}/h$). Middle: fractional accuracy of the DK14 model. Right: comparison between the values of the logarithmic slope as computed from the DK14 fits (colored lines) and those computed through a Savitzky-Golay filter (black lines). The accuracy of the DK14 is generally better than 5% in agreement with Diemer & Kravtsov (2014). However, the DK14 model fits do not capture the appearance of the second caustic (red arrows). We will show that this can lead to difficulties when using DK14 to fit for the minimum of the log-slope of ρ^{3D} in low accretion rate bins.

2.3 Fiducial Density, Suhalo, and Weak Lensing Profiles

We use `Halotools` (Hearin et al. 2017) to compute stacked 3D density, subhalo, and weak lensing profiles for our fiducial halo sample. The density profile can be computed from the cross-correlation function as:

$$\langle \rho(r) \rangle = \bar{\rho}_m (\xi(r)_{12} + 1), \quad (3)$$

where $\bar{\rho}_m$ is the mean matter density of the universe, and $\xi(r)_{12}$ is the two-point cross-correlation function computed with the `Halotools` function `tpcf`. To compute 3D density profiles (ρ^{3D}) we cross-correlate host halos with dark matter particles, while for the 3D subhalo profiles (ρ_{sub}^{3D}) we cross-correlate host halos with subhalos.

We compute the weak lensing profile ($\Delta\Sigma$) for our fidu-

cial halo sample by measuring the excess surface density of dark matter particles in cylinders surrounding host halos using the `Halotools` function `DeltaSigma`.

2.4 Fitting Profiles with the DK14 model

We model the 3D density, subhalo, and weak lensing profiles with DK14 using the python toolkit `COLLOSSUS` (Diemer 2018). The functional form of the 3D density profile is shown in Equation 1. The projected surface mass density, $\Sigma(R)$, is the integral of the density profile along the line of sight:

$$\Sigma(R) = \int_{-h_{\text{max}}}^{h_{\text{max}}} \rho \sqrt{R^2 + h^2} dh, \quad (4)$$

where h_{max} is the maximum line of sight integration length,

Parameter	Priors
$\log(\rho_s)$	$\mathcal{U}(4, 8) \log(\text{M}_\odot h^2/\text{kpc}^3)$
$\log(r_t)$	$\mathcal{U}(2, 4) \log(\text{kpc}/h)$
$\log(r_s)$	$\mathcal{U}(0, 4) \log(\text{kpc}/h)$
$\log(\alpha)$	$\mathcal{N}(-0.67, 0.16)$
β	$\mathcal{N}(4, 0.1)$
γ	$\mathcal{N}(6, 0.1)$
$\log(\rho_0)$	$\mathcal{U}(0, 0.5) \log(\text{M}_\odot h^2/\text{kpc}^3)$
s_e	$\mathcal{U}(1, 10)$

Table 1. Priors used to fit DK14 to the 3D density and weak lensing profiles.

namely $10^8 \text{kpc}/h$. The excess surface mass density, $\Delta\Sigma(R)$, is then:

$$\Delta\Sigma(R) = \frac{1}{\pi R^2} \int_0^R 2\pi r \Sigma(r) dr - \Sigma(R). \quad (5)$$

Following Baxter et al. (2017) and Chang et al. (2018) we use a Bayesian approach to fit DK14 to $\rho^{3\text{D}}$, $\rho_{\text{sub}}^{3\text{D}}$, and $\Delta\Sigma$. We adopt similar priors to Chang et al. (2018) (see Table 1). Most of the parameters have wide uniform priors. We use Gaussian priors on α motivated by Gao et al. (2008), and on β and γ as recommended by Diemer & Kravtsov (2014). We sample the posterior parameter space with a Markov Chain Monte Carlo (MCMC) analysis implemented in `emcee` (Foreman-Mackey et al. 2013). We assess for convergence using trace plots and Kolmogorov-Smirnov statistic. Once the chains are converged, we rebuild the profiles using the parameters chosen by the chain in each iteration. From these model profiles, we compute the posterior distribution of R_{DK14} (minimum of the logarithmic slope).

2.5 Summary of Notation

To summarize, throughout this paper, we use the following notation for different R_{sp} measurements.

- R_{SPARTA}^{50} : 50th percentile of R_{sp} measured with SPARTA from the particle trajectories of L500-Planck and matched with our halo sample (see Section 2.2.1). Similarly, R_{SPARTA}^{67} denotes the 67th percentile and so on and so forth.
- R_{SG} : location of the steepest slope of $\rho^{3\text{D}}$ measured with SG.
- R_{DK14} : location of the steepest slope of $\rho^{3\text{D}}$ measured with DK14.
- R_{sub} : location of the steepest slope of $\rho_{\text{sub}}^{3\text{D}}$.
- $R_{\text{SG,sub}}$: location of the steepest slope of $\rho_{\text{sub}}^{3\text{D}}$ measured with SG.
- $R_{\text{DK14,sub}}$: location of the steepest slope of $\rho_{\text{sub}}^{3\text{D}}$ measured with DK14.

3 RESULTS

We now examine how R_{sp} estimates computed from density, weak lensing, and subhalo profiles compare to the distribution of R_{sp} values measured with SPARTA.

3.1 Splashback Radius Estimate from 3D Density Profiles

We measure the 3D density profiles for our fiducial sample in bins of accretion rate (Figure 1) following the methodology described in Section 2.3. The profiles are shown in Figure 2, which displays $\rho^{3\text{D}}$ and the log-slopes of $\rho^{3\text{D}}$ for halos binned by accretion rate. Figure 2 shows that the minimum of the log-slopes of $\rho^{3\text{D}}$ shifts to smaller scales and becomes deeper with increasing Γ_{dyn} . For $\Gamma_{\text{dyn}} < 1.8$, however, a second minimum is apparent at radii smaller than the splashback radius. This feature is a second caustic: a second sharp drop in $\rho^{3\text{D}}$. Caustics are caused by particle orbits that pile up at the same location at the apocenters of their orbits (Adhikari et al. 2014). The second caustic corresponds to the location where particles reach the apocenter of their second orbit. The trends in Figure 2 are in agreement with results from previous work (Diemer & Kravtsov 2014; Adhikari et al. 2014; More et al. 2015; Diemer et al. 2017).

We fit the 3D density profiles in Figure 2 with DK14 and SG and display the results in Figure 3. Diemer & Kravtsov (2014) showed that DK14 fits the data with a fractional accuracy of 5 to 10%. Figure 3 shows that indeed, the accuracy of the DK14 fits is, in general, better than 5%. However, the model does not capture the appearance of the second caustic that arises in the lower accretion rate bins ($\Gamma_{\text{dyn}} < 1.8$).

Finally, in Figure 4, we study how R_{sp} estimated from 3D density profiles compares to the apocentric radius of particles computed with SPARTA. Particles infalling onto halos will have a range of apocentric radii. This means that a given halo will not have a single fixed R_{sp} , but rather a *distribution* of values. For this reason, SPARTA provides the 50th, 63rd, 75th and 87th percentile of the apocentric radius of individual particles. Each of our bins in $M_{200\text{m}}$ and Γ_{dyn} is comprised of a sample of halos. Therefore, each bin in $M_{200\text{m}}$ and Γ_{dyn} will have a distribution of values for a given percentile. This distribution is indicated by the shaded regions in Figure 4. For example, the upper left panel of Figure 4 compares R_{DK14} and R_{SG} with R_{SPARTA}^{50} . The width of the green shaded region represents the 1σ distribution of R_{SPARTA}^{50} , and the solid green line in the middle is the mean value of R_{SPARTA}^{50} in each accretion rate bin.

Figure 4 shows that the steepest slope of $\rho^{3\text{D}}$ agrees with R_{SPARTA}^{75} for the higher accretion bins ($\Gamma_{\text{dyn}} > 2.5$), and with R_{SPARTA}^{87} for the lower accretion bins ($\Gamma_{\text{dyn}} < 2.5$). Furthermore, R_{SG} and R_{DK14} agree throughout all accretion bins except in the lowest one ($\Gamma_{\text{dyn}} < 1.1$). Unlike SG, DK14 largely underestimates the steepest slope for the lowest accretion bin. This is due to the second caustic that becomes apparent in the lower accretion bins ($\Gamma_{\text{dyn}} < 1.8$) and is most prominent in the lowest bin. Thus, using the steepest slope as the R_{sp} estimate for halos with low accretion rates will lead to biased measurements.

3.2 Splashback Radius Estimate from 3D Subhalo Profiles

Given that in observations, we measure satellite (and thus subhalo) profiles, we now investigate how the steepest slope of $\rho_{\text{sub}}^{3\text{D}}$ varies with accretion rate. We focus in particular on subhalos that roughly correspond to a DESI-like selection

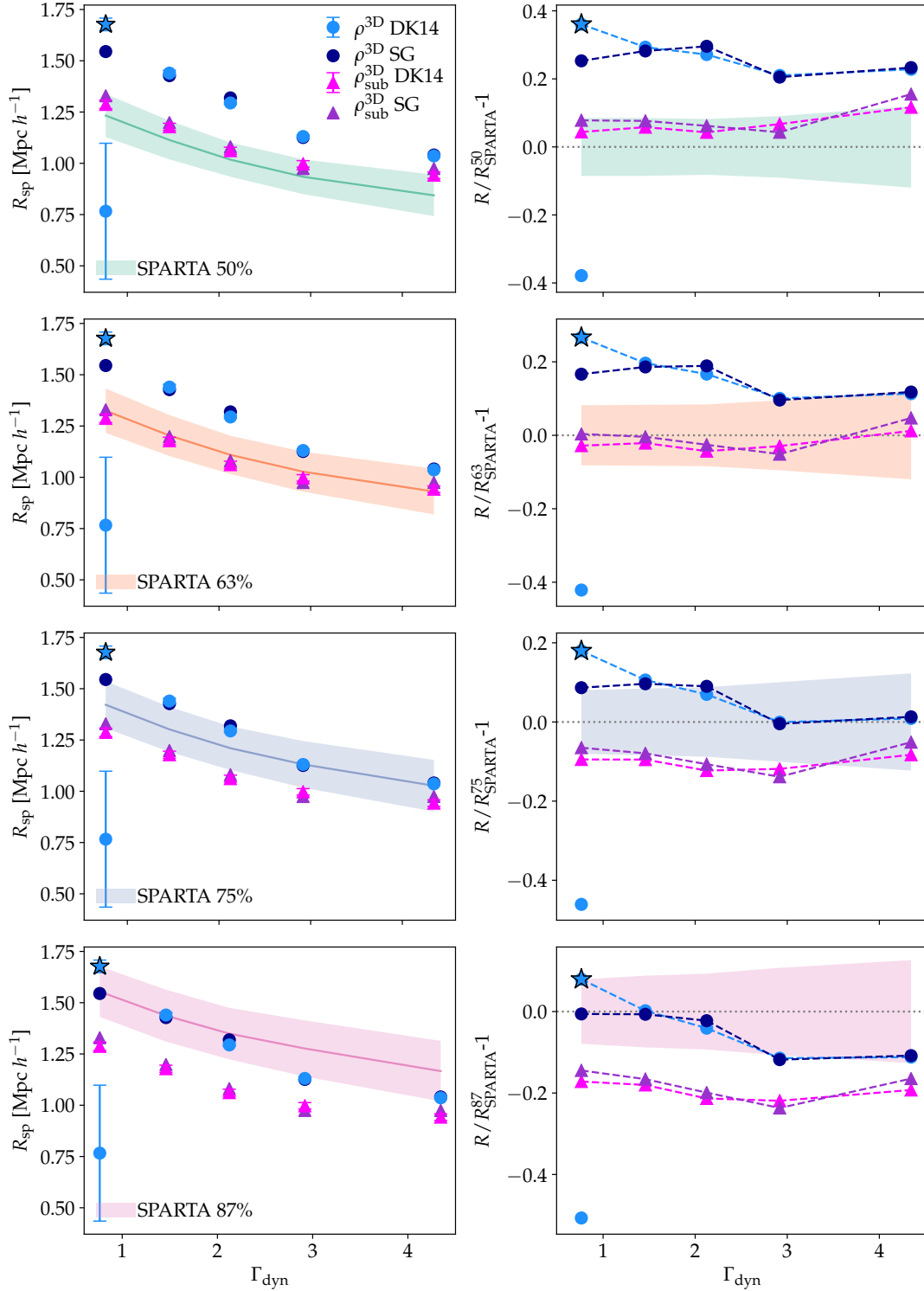


Figure 4. Left: R_{sp} estimates from $\rho^{3\text{D}}$ (circles) and $\rho^{3\text{D}}_{\text{sub}}$ (triangles) using both the DK14 model fits and Savitzky-Golay. Rows from top to bottom compare these R_{sp} estimates with different percentiles of R_{SPARTA} (shaded regions). Solid lines represent the mean value of the percentile for each bin in $M_{200\text{m}}$ and Γ_{dyn} . The width of the shaded region is the 1σ spread of percentile values. The blue star displays the value of R_{sp} for the lowest accretion rate bin when selecting the higher peak in the bimodal distribution of the posterior (Figure 7). Right: ratio of estimated R_{sp} values to different percentiles of R_{SPARTA} . The steepest slope of $\rho^{3\text{D}}$ does not correspond to any single percentile values from SPARTA. Instead, it matches R_{SPARTA}^{75} for the higher accretion bins ($\Gamma_{\text{dyn}} > 2.5$), and R_{SPARTA}^{87} for the lower accretion bins ($\Gamma_{\text{dyn}} < 2.5$). On the other hand, the steepest slope of $\rho^{3\text{D}}_{\text{sub}}$ matches R_{SPARTA}^{63} consistently across all Γ_{dyn} bins. Finally, DK14 fails in the low accretion regime. This is due to the appearance of the second caustic in the density profile, which causes a bimodal posterior distribution.

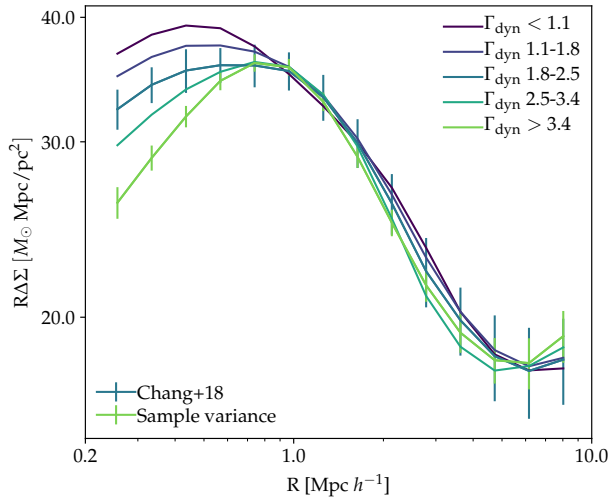


Figure 5. Weak lensing profiles for the same halo samples as in Figure 2. Blue error bars correspond to the errors reported by Chang et al. (2018) for the DES Y1 data. Green error bars are computed by resampling over host halos in MDPL2.

(see Section 2.1). We measure R_{sub} by fitting the subhalo profiles with DK14 and SG. Errors are computed by resampling over host halos. Figure 4 compares R_{sub} estimated from the steepest slope of $\rho_{\text{sub}}^{3\text{D}}$ to R_{sp} estimated from particle apocenters. Figure 4 conveys that R_{sub} agrees with R_{SPARTA}^{63} across all accretion bins. This shows that R_{sub} is not susceptible to fitting artifacts due to the second caustic. Additionally, R_{sub} does not trace the steepest slope of the 3D density profiles. The systematically lower R_{sub} may indicate evidence of the dynamical friction drag due to the massive subhalos in our sample (Adhikari et al. 2016).

3.3 Splashback Radius Estimate from Weak Lensing

Gravitational lensing is potentially the most direct method for detecting R_{sp} since it traces the mass profile of dark matter halos and will not be affected by issues such as dynamical friction that can bias R_{sub} . However, weak lensing only measures the projection of $\rho^{3\text{D}}$. We expect projection effects to wash out the splashback feature, making the minimum of the logarithmic slope around R_{sp} broader and, therefore, harder to constrain. Figure 5, displays the weak lensing profiles of our fiducial halo mass sample binned by accretion rate using the same bins as in Figure 2.

We fit the fiducial weak lensing profiles from MDPL2 with DK14 using, in one case, the sample variance errors of the MDPL2 simulation, and in the other case, the observational error bars from reported by Chang et al. (2018). Figure 6 shows R_{sp} posteriors for weak lensing profiles using MDPL2 sample variance errors (left panel) and DES Y1 error bars (right panel). Profiles are color-coded by accretion rate as in Figure 5. Posteriors in both panels overlap with each other. Although both the 3D density and weak lensing profiles are built from the same samples (Figure 1), the R_{sp} correlation with accretion rate is less constrained in the weak lensing profiles. This is due to the projection effects in-

troducted when computing $\Delta\Sigma$ in projected space. The right panel shows that R_{sp} posteriors for the lensing profiles modeled with DES Y1 error bars are even less constrained than those with jackknife resampling. Because observational error bars are naturally larger than the jackknife ones, they put worse constraints on the posteriors.

4 DISCUSSION

4.1 Accuracy of R_{sp} with Estimators

In Figure 4 we compared R_{sp} from particle dynamics to the location of the steepest slope in 3D density and subhalo profiles. For the density profiles, the location of the steepest slope for the higher accretion bins ($\Gamma_{\text{dyn}} > 2.5$) converges with R_{SPARTA}^{75} , while for the lower accretion bins ($\Gamma_{\text{dyn}} < 2.5$), it converges with R_{SPARTA}^{87} . Moreover, we find that the SG method and the DK14 profile fitting routine provide consistent results for all accretion bins, except for $\Gamma_{\text{dyn}} < 1.1$. Posteriors of R_{sp} estimates in 3D density profiles in Figure 7 show that the lowest accretion bin has a bimodal distribution. All of these effects are due to the second caustic apparent in the logarithmic density slopes of slowly accreting halos, which is most clearly seen in the lowest accretion bin ($\Gamma_{\text{dyn}} < 1.1$). As this feature becomes evident, the location of the steepest slope matches a higher percentile of R_{SPARTA} . Because the second caustic is not modeled by DK14, the R_{sp} posterior for the lowest accretion bin in Figure 7 is bimodal. The first peak is located around 0.7 Mpc/h, while the second around 1.7 Mpc/h. The two modes of the posterior correspond to the first and second caustic we see in the logarithmic slope of the lowest accretion bin (Figure 3). However, only the one located at 1.7 Mpc/h corresponds to the steepest slope of the density profile. In conclusion, the location of the steepest slope of the density profile does not correspond to a single percentile of R_{SPARTA} . Instead, the matched R_{SPARTA} percentile changes with accretion rate due to the appearance of the second caustic.

Figure 4 also shows that we will be able to detect R_{sp} through 3D subhalo profiles with DESI Y1. When subhalos are used to trace the halo profile, we find that the R_{sp} estimated from subhalo profiles is smaller than that from 3D density profiles. The location of the steepest slope in subhalo profiles in Figure 4 matches R_{SPARTA}^{63} consistently in all accretion bins. This may be due to the dynamical friction drag of the most massive subhalos in our sample. It is well known that dynamical friction causes the most massive subhalos to sink to the center of the host. More et al. (2016) and Adhikari et al. (2016) showed that this effect also translates into the apocentric radii of subhalos. They concluded that R_{sp} from subhalos for a massive subhalo sample is smaller than R_{sp} from particles for the same host halo. Figure 4 shows a similar qualitative effect as More et al. (2016) and Adhikari et al. (2016). Given that the mass of the subhalos in our sample is greater than 1% of the host mass, the dynamical friction drag is significant in our R_{sub} measurements (Adhikari et al. 2016). However, a more rigorous study would be required to prove that dynamical friction is indeed the primary cause of the offset seen in Figure 4.

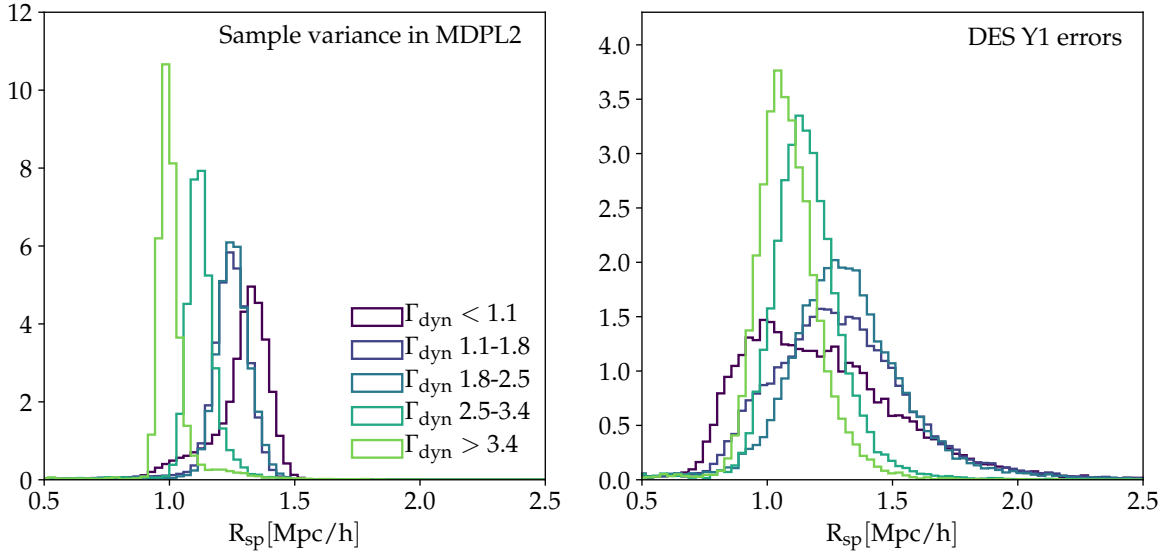


Figure 6. Steepest slope posteriors for $\Delta\Sigma$ measured with DK14. Posteriors on the left panel are computed using error bars corresponding to sample variance of the MDPL2 simulation, while those on the right are constrained with DES Y1 error bars. Different colors represent different accretion rate bins as in Figure 2. Although ρ^{3D} and $\Delta\Sigma$ are built from the same halo sample, the location of the steepest slope for $\Delta\Sigma$ is less constrained than for ρ^{3D} (Figure 7). This is because of the projection effects introduced when measuring $\Delta\Sigma$. The right-hand panel shows that the DES Y1 lensing errors are too large to allow for the detection of the $R_{sp} - \Gamma_{dyn}$ connection. Conversely, this also means that DES Y1 constraints on R_{sp} will not be affected by any possible Γ_{dyn} selection effects.

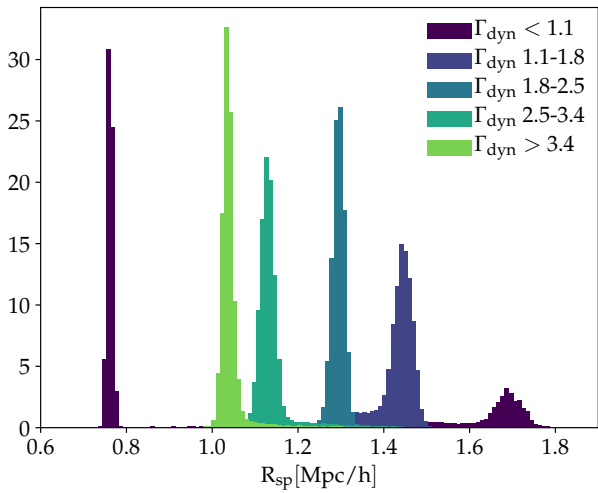


Figure 7. Posteriors of the steepest slope of ρ^{3D} measured with DK14. Different colors represent different bins in accretion rate, corresponding to the same color scheme as in Figure 2. The lowest accretion bin ($\Gamma_{dyn} < 1.1$) displays a bimodal distribution of the steepest slope posterior.

4.2 On Detecting the Correlation Between R_{sp} and Γ_{dyn}

One of the most intriguing potential applications of the splashback radius is to observe the accretion rate of halos. The correlation between R_{sp} and Γ_{dyn} has already been proven theoretically (Adhikari et al. 2014; Shi 2016) and studied in simulations (Diemer & Kravtsov 2014; More et al.

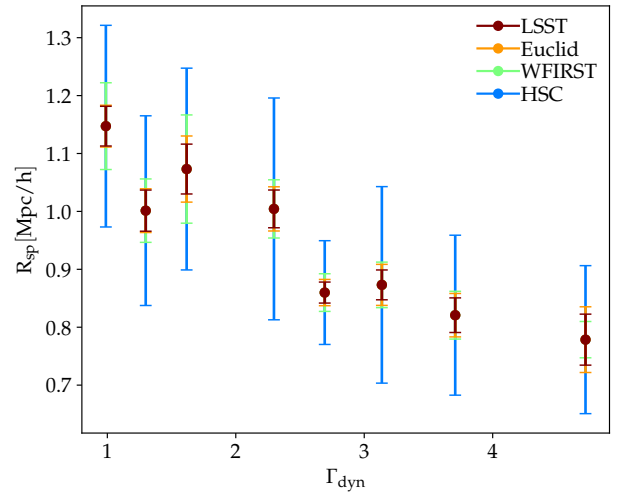


Figure 8. Splashback-accretion rate relation when considering forecast weak lensing error bars from future surveys. LSST and Euclid give the best constraint for the correlation between R_{sp} and Γ_{dyn} .

2015; Diemer 2017; Diemer et al. 2017). More importantly, this correlation is based on basic gravitational physics and should, in principle, be detectable in real data, if tracers of not only halo mass but also Γ_{dyn} can be established. However, current DES Y1 weak lensing errors are too large to constrain the $R_{sp} - \Gamma_{dyn}$ trend (see Figure 6). The reason why this is challenging is that lensing measures a projected quantity which washes out the splashback feature. Furthermore, the signal itself is intrinsically noisy and introduces

more uncertainty in the R_{sp} measurement than in the case of density profiles. This raises the need for better data to constrain the $\Gamma_{\text{dyn}} - R_{\text{sp}}$ relation with weak lensing profiles.

Here we assume a perfect (zero scatter) observational tracer of halo mass and accretion rate. Future work will discuss noisy tracers and their impact on the detectability of the $R_{\text{sp}} - \Gamma_{\text{dyn}}$ trend. Figure 8 shows how precisely and accurately one can measure the splashback radius in bins of Γ_{dyn} for HSC, and future surveys such as LSST, Euclid, and WFIRST. We compute the lensing error bars for each of these surveys using the same methodology as the one introduced in Singh et al. (2017) and applied in Leauthaud et al. (2019). Forecast error bars include all the terms needed to describe a Gaussian covariance and assume a perfect observational tracer of accretion rate. We do not account for effects due to selection or survey masks. Furthermore, the forecast error bars do not account for the non-gaussian covariance, and hence the signal to noise they predict is somewhat overestimated. The halo bin considered is the same as throughout the rest of this paper, namely $10^{13.8} - 10^{14.1} M_{\odot}/h$.

In order to study how well we can constrain the $R_{\text{sp}} - \Gamma_{\text{dyn}}$ correlation in future surveys, we perform a linear fit of the data points in Figure 8. The best fit slopes are -0.10 ± 0.02 for HSC, -0.11 ± 0.02 for WFIRST, -0.09 ± 0.01 for Euclid, and -0.09 ± 0.01 for LSST. All the slopes have a significance higher than 5σ , with Euclid and LSST giving the tightest constraint. Thus, upcoming weak lensing surveys may be able to constrain the $\Gamma_{\text{dyn}} - R_{\text{sp}}$ relation. However, this assumes a perfect observational tracer of Γ_{dyn} . Further work will be necessary to construct and characterize observational tracers of Γ_{dyn} .

5 SUMMARY AND CONCLUSIONS

In this paper, we have studied the accuracy and precision to which we can detect the splashback radius in simulated 3D density, subhalo, and weak lensing profiles. Our main goals are to (1) study how well the location of the steepest slope compares with the splashback radius from particle dynamics and (2) how precisely we can detect the splashback radius with weak lensing data given current and future surveys. We use the MDPL2 simulation to build fiducial density, subhalo, and weak lensing profiles binned by halo mass accretion rate. We measure the steepest slope parametrically, through the DK14 model, and non-parametrically, through the SG algorithm. Finally, we compare these measurements with R_{sp} from particle dynamics measured with SPARTA. Our main conclusions are the following:

(i) The steepest slope from 3D density profiles does not agree with a single percentile of particle apocenters as measured by SPARTA. The steepest slope roughly corresponds to R_{SPARTA}^{87} at low accretion rates and R_{SPARTA}^{75} at high accretion rates.

(ii) For halo samples with $\Gamma_{\text{dyn}} < 1.1$, DK14 predicts a bimodal distribution of the steepest slope when considering the 3D density profile. This is because of the second caustic that appears in the density profiles of slowly accreting halos.

(iii) It will be possible to detect R_{sp} using a DESI Y1-like subhalo selection through 3D subhalo profiles.

(iv) R_{sp} estimates from 3D subhalo profiles match R_{SPARTA}^{63} and are smaller than the R_{sp} estimates from 3D density profiles across all accretion bins. This might be due to the dynamical friction drag of the massive subhalos in our sample.

(v) We cannot constrain the $R_{\text{sp}} - \Gamma_{\text{dyn}}$ trend with DES Y1 errors. However, given an ideal observable tracer of accretion rate (zero scatter), we will be able to detect the $R_{\text{sp}} - \Gamma_{\text{dyn}}$ trend with other current and future surveys such as HSC, WFIRST, Euclid and LSST. Euclid and LSST will provide the best constraints on this relation.

There is an exciting possibility that upcoming weak lensing surveys may be able to constrain the $R_{\text{sp}} - \Gamma_{\text{dyn}}$ relation. Further work will be required to construct and characterize observational tracers of Γ_{dyn} .

ACKNOWLEDGEMENTS

This research was supported in part by the National Science Foundation under Grant No. NSF PHY-1748958. This material is based on work supported by the UD Department of Energy, Office of Science, Office of High Energy Physics under Award Number de-sc0019301. AL acknowledges support from the David and Lucille Packard Foundation, and the Alfred .P Sloan foundation. EX acknowledges the generous support of Mr. and Mrs. Levy via the LEVY fellowship.

REFERENCES

- Adhikari S., Dalal N., Chamberlain R. T., 2014, *J. Cosmology Astropart. Phys.*, 2014, 019
- Adhikari S., Dalal N., Clampitt J., 2016, *J. Cosmology Astropart. Phys.*, 2016, 022
- Adhikari S., Sakstein J., Jain B., Dalal N., Li B., 2018, *J. Cosmology Astropart. Phys.*, 2018, 033
- Aihara H., et al., 2018, *PASJ*, 70, S8
- Banerjee A., Adhikari S., Dalal N., More S., Kravtsov A., 2019, arXiv e-prints, p. arXiv:1906.12026
- Baxter E., et al., 2017, *ApJ*, 841, 18
- Behroozi P. S., Wechsler R. H., Wu H.-Y., 2013a, *ApJ*, 762, 109
- Behroozi P. S., Wechsler R. H., Wu H.-Y., Busha M. T., Klypin A. A., Primack J. R., 2013b, *ApJ*, 763, 18
- Bertschinger E., 1985, *ApJS*, 58, 39
- Busch P., White S. D. M., 2017, *MNRAS*, 470, 4767
- Chang C., et al., 2018, *ApJ*, 864, 83
- Chue C. Y. R., Dalal N., White M., 2018, *J. Cosmology Astropart. Phys.*, 2018, 012
- Contigiani O., Hoekstra H., Bahé Y. M., 2019, *MNRAS*, 485, 408
- DESI Collaboration et al., 2016, arXiv e-prints, p. arXiv:1611.00036
- Diemer B., 2017, *ApJS*, 231, 5
- Diemer B., 2018, *ApJS*, 239, 35
- Diemer B., Kravtsov A. V., 2014, *ApJ*, 789, 1
- Diemer B., Kravtsov A. V., 2015, *ApJ*, 799, 108
- Diemer B., Mansfield P., Kravtsov A. V., More S., 2017, *ApJ*, 843, 140
- Fillmore J. A., Goldreich P., 1984, *ApJ*, 281, 1
- Foreman-Mackey D., Hogg D. W., Lang D., Goodman J., 2013, *PASP*, 125, 306
- Gao L., Navarro J. F., Cole S., Frenk C. S., White S. D. M., Springel V., Jenkins A., Neto A. F., 2008, *MNRAS*, 387, 536
- Gunn J. E., Gott J. Richard I., 1972, *ApJ*, 176, 1
- Hearin A. P., et al., 2017, *AJ*, 154, 190

- Ivezic Z., et al., 2008, *Serbian Astronomical Journal*, 176, 1
- Laureijs R., et al., 2011, arXiv e-prints, p. arXiv:1110.3193
- Leauthaud A., Singh S., Luo Y., Ardila F., Greco J. P., Capak P., Greene J. E., Mayer L., 2019, arXiv e-prints, p. arXiv:1905.01433
- Mansfield P., Kravtsov A. V., 2019, arXiv e-prints, p. arXiv:1902.00030
- Mansfield P., Kravtsov A. V., Diemer B., 2017, *ApJ*, 841, 34
- More S., Diemer B., Kravtsov A. V., 2015, *ApJ*, 810, 36
- More S., et al., 2016, *ApJ*, 825, 39
- Navarro J. F., Frenk C. S., White S. D. M., 1996, *ApJ*, 462, 563
- Planck Collaboration et al., 2014, *A&A*, 571, A31
- Prada F., Klypin A. A., Cuesta A. J., Betancort-Rijo J. E., Primatech J., 2012, *MNRAS*, 423, 3018
- Rykoff E. S., et al., 2014, *ApJ*, 785, 104
- Savitzky A., Golay M. J. E., 1964, *Analytical Chemistry*, 36, 1627
- Shi X., 2016, *MNRAS*, 459, 3711
- Shin T., et al., 2019, *MNRAS*, 487, 2900
- Singh S., Mandelbaum R., Seljak U., Slosar A., Vazquez Gonzalez J., 2017, *MNRAS*, 471, 3827
- Spergel D., et al., 2013, arXiv e-prints, p. arXiv:1305.5422
- Umetsu K., Diemer B., 2017, *ApJ*, 836, 231
- Villarreal A. S., et al., 2017, *MNRAS*, 472, 1088
- Khakaj E., Leauthaud A., Diemer B., Behroozi P., 2019, *Research Notes of the AAS*, 3, 169
- Zürcher D., More S., 2019, *ApJ*, 874, 184